Catalysis Letters
https://doi.org/10.1007/s10562-020-03520-5

Ru Nanoparticles on a Sulfonated Carbon Layer Coated SBA-15 for Catalytic Hydrogenation of Furfural into 1, 4-pentanediol

Kai Cui[1] · Wei Qian[1] · Zhengjiang Shao[1] · Xiuge Zhao[1] · Honghui Gong[1] · Xinjia Wei[1] · Jiajia Wang[1] · Manyu Chen[1] · Xiaoming Cao[1] · Zhenshan Hou[1]

Received: 3 September 2020 / Accepted: 24 December 2020

Abstract

Furfural (FFR) is one of the most important biomass-derived chemicals. Its large-scale availability calls for the exploration of new transformation methods for further valorization. Herein, we demonstrate that Ru nanoparticles (Ru NPs)-supported on a sulfonated carbon layer coated SBA-15 can be employed as an efficient bi-functional catalyst for one step conversion of FFR into 1,4-pentanediol (1,4-PeDO). The optimum bi-functional catalyst can afford the full the conversion of FFR and 86% selectivity to 1,4-PeDO. The catalysts have been characterized thoroughly by using a complementary combination of powder X-ray diffraction, N_2 adsorption–desorption, scanning/transmission electron microscopy, Fourier transform infrared spectroscopy, elemental analysis, and X-ray photoelectron spectroscopy. The characterization revealed that acidic groups ($–SO_3H$) have been introduced on the surface of the carbon layer coated SBA-15 support after sulfonation with 98% H_2SO_4 and the surface acidity can be tuned facilely by the sulfonating time. Meantime, Ru(0) sites was highly dispersed via an impregnation and sequential reduction and directly adjacent to the surface $–SO_3H$ group. There existed an electronic interaction between Ru(0) sites and sulfonic groups, in which the electronic transfer from sulfonic sites to Ru(0) sites occurred. Brönsted acid sites ($–SO_3H$) have a significant influence on the FFR conversion and the selectivity to 1,4-PeDO. The ordered mesoporous structure, the appropriate density of acid sites and the electron-rich Ru(0) sites accounted for the the excellent performance of the catalyst for an efficient production of 1,4-PeDO from FFR.

Kai Cui and Wei Qian have contributed equally.

Supplementary Information The online version of this article (https://doi.org/10.1007/s10562-020-03520-5) contains supplementary material, which is available to authorized users.

✉ Xiaoming Cao
xmcao@ecust.edu.cn

✉ Zhenshan Hou
houzhenshan@ecust.edu.cn

[1] Key Laboratory for Advanced Materials, Research Institute of Industrial Catalysis, School of Chemistry and Molecular Engineering, East China University of Science and Technology, Shanghai 200237, China

Published online: 21 January 2021

Graphic Abstract

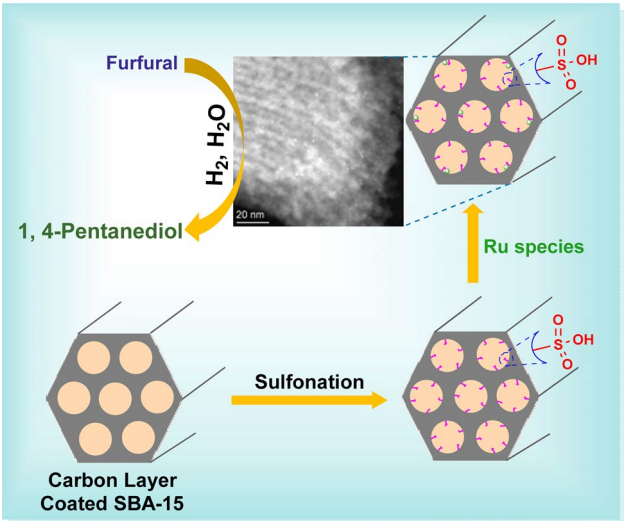

Keywords Furfural · Hydrogenation · SBA-15 · Carbon layers · Sulfonation, Ru

1 Introduction

Development of new methodologies for biomass transformation is gaining extensive attention. As biomass, a viable resource of carbon and extensively available in nature, has shown its potential for the production of carbon-based energy sources and several valuable platform chemicals, it can probably replace or provide an alternative to the currently used fossil fuel and high value-added fine chemicals [1–5]. To utilize the biomass effectively, efficient technologies are needed for the selective tailoring of oxygen content and functionality of the biomass-derived raw materials. C5 and C6 sugars are the main components of biomass feedstock [6]. Furfural (FFR) is already produced on an industrial scale from these sugars via acidic hydrolysis, and the vast majority of FFR can be converted into furfuryl alcohol (FAL), tetrahydrofurfuryl alcohol (THFA), and 2-methylfuran (2-MeTF), which are used as solvents, plasticisers, monomers in the production of resins, in the agrochemicals industry, or as gasoline blends. Notably, FAL and its derivatives can also be transformed into pentanediols (PeDOs) such as 1, 2-, 1, 4- or 1, 5-pentanediol (PeDO), which can be employed as a component of disinfectants or microbicides, as an ingredient of various cosmetic products, and as a monomer of polyesters and polyurethanes [7–10].

Thus far, the selective hydrogenolysis of FFR or its derivatives at the C-O bonds in the furan ring to produce PeDOs mainly focused on using supported catalysts of group VIII precious metals (Ru, Pt, Rh, and Ir etc.) [10–14]. In particular, low-valence metallic oxides (such as ReO_x, MoO_x, VO_x or WO_x)-incorporated Rh and Ir catalysts attracted much attention for the hydrogenolysis of FFR or derivatives to synthesize 1,2- or 1,5-PeDO with excellent selectivity [15–19]. Nevertheless, there were a few reports on a catalytic production of 1,4-PeDO from hydrogenolysis of FFR. It is worth noting that the previously reported catalysts for the synthesis of 1,4-PeDO from FFR or FAL were carried out under harsh reaction conditions. For example, the direct conversion of FFR could give 1,2-PeDO (16% yield), 1,5-PeDO and 1,4-PeDO (6.2% yield) in ethanol over the spinel-type Pt/$CoAl_2O_4$ catalyst at 413 K, 1.0 MPa H_2 for 24 h [20]. The Rh-Ir-ReO_x/SiO_2 catalyst was also used for the selective hydrogenation of FFR in water, which produced only 13% yield of 1,4-PeDO at 393 K, 8.0 MPa H_2 for 24 h [11]. Thereafter, the yield of 1,4-PeDO was reported to increase up to *ca.* 30% considerably on Pd-Ir-ReO_x/SiO_2 catalyst under the similar reaction conditions [21].

Although many reaction routes have been reported to afford a significant yield of 1,4-PeDO, such as hydrogenation of levulinic acid (LA), γ-valerolactone (GVL) or ethyl levulinate in the presence of heterogeneous noble metal-based catalysts, the reaction could normally occur at > 473 K and 6–15 MPa H_2 [22–26]. Hence, the development of the heterogeneous catalysts for the effective synthesis of PeDOs, especially 1,4-PeDO, from C5-furan compounds under more mild condition is a highly promising and challenging work. Most recently, Zhang and co-workers reported the catalytic conversion of FFR to 1,4-PeDO over Ru/CMK-3 catalysts in H_2O at 353 K. The

weak acid sites were provided by the positively charged Ru species and the water-dissolved pressurized CO_2 for the reaction [13]. Thereafter, they found that in combination with Amberlyst-15, the Ru-6.3FeO_x/AC catalyst could afford a 1,4-PeDO yield of 86% [27]. Besides, Shimazu' group has also reported novel Ni–Sn alloy catalysts that could convert FFR to 1,4-PeDO under the condition of 3.0 MPa, 433 K, in which the effects of the solvent, reaction temperature and H_2 pressure on catalytic activity have been investigated [28]. However, the current catalytic systems for FFR hydrogenation normally show a weak and moderate acidity [13], and in some cases either the acidic medium or other additives are needed during the reactions. It has been reported that Brönsted acid sites could facilitate the hydrogenation of FFR by the hydrolytic ring-opening and lactonization reaction [29–31], but the effects of the density of Brönsted acid sites on the production of 1,4-PeDO from FFR remained to be clarified.

As a cheaper Pt-group metal, ruthenium (Ru) is a highly competitive alternative as a catalyst component. Notably, Ru-based catalysts displayed high catalytic efficiency for hydrogenation and also C-O bond cleavage under the aqueous condition [32, 33]. In the previous work, we have found that the carbon layer coated SBA-15 (C-SBA-15) is hydrothermally stable in aqueous-hydrogenation and showed a high BET surface area (more than 500 $m^2 \cdot g^{-1}$) [34]. Based on our previous work, we attempted initially to carry out the hydrogenation of FFR by using Ru/C-SBA-15 as a catalyst, but unfortunately the product distribution is rather wide and a large amount of the products (THFA) from furan ring hydrogenation was detected. This revealed that the acid sites could be crucial for the formation of diols while the Ru/C-SBA-15 catalyst lacked the acid sites. Herein, in this work we have designed a metal–acid bi-functional catalyst. For this purpose, the sulfonated carbon layer coated SBA-15 (SC-SBA-15) was obtained by sulfonating C-SBA-15 with 98% concentrated sulfuric acid. Sequentially, Ru sites were introduced into the modified support by impregnation and reduction to attain the bi-functional catalysts containing both metal sites and acid sites. Notably, the density of acid sites on the catalysts was highly dependent on the sulfonating time. The further characterization on the properties of catalytic active sites has provided a deep insight into the relationship between the metal–acid sites and catalytic performance. Additionally, the influences of reaction parameters on the product selectivity along with the reaction kinetics using MATLAB program were studied. Based on these results above, reaction pathway has been also elucidated.

2 Experimental

2.1 Materials

All chemicals and solvents were commercially available and used as received without further purification. Ruthenium(III) chloride ($RuCl_3 \cdot nH_2O$, Ru, 37.01%), sucrose, NaCl (99%), NaOH (99%) and phenolphthalein were from Sinopharm Chemical Reagent Co. Ltd. Concentrated sulfuric acid (98%), hydrochloric acid (38%) tetraethyl orthosilicate (TEOS, 98.00%), ethanol (Anhydrous 99.99%), pluronic P123 and all the substrates were purchased from Shanghai Tian Lian Chemical Technology Co. Ltd. High purity N_2 (99.99%) and H_2 (99.99%) were supplied by Shang Nong Gas Factory. Commercial Ru/AC (5 wt%) was obtained from Sino-pharm Chemical Reagent Co. Ltd. Furfural (99%), furfuryl alcohol (99%), tetrahydrofurfuryl alcohol (98%), 1,4-pentanediol (97%), 5-hydroxy-2-pentanone (95%), diethyl ether and n-butanol (99%) were obtained from Aladdin. The distilled water was used in all experiments.

2.2 Catalyst Preparation

2.2.1 Preparation of SC-SBA-15

SBA-15 was synthesized according to the previous report (the details for the synthesis of SBA-15 are given in supporting information) [35]. The carbon layer coated SBA-15 was synthesized using the following procedure: 0.5 g sucrose were dissolved in deionized water and then 1 g SBA-15 was added into the mixture. The resulting aqueous suspension stirred in an open evaporating dish at 50 °C until the water evaporated and a white solid was obtained. The white solid was ground, transferred into a quartz boat, followed by pyrolyzing in a tube furnace under high purity nitrogen flow at 550 °C for 4 h with a ramp rate of 2.5 °C·min^{-1}. The carbon coated SBA-15 was denoted as C-SBA-15. Next, 1 g C-SBA-15 was added to 15 mL of concentrated sulfuric acid (H_2SO_4, 98%) in a 50 mL glass tube, the resulting reaction mixture was ultra-sonicated for 2 h in ambient conditions, and then was heated under the protection of nitrogen flow (10 mL·min^{-1}) at 110 °C for another 3, 6, 9 h with stirring. The reaction mixture was cooled to ambient temperature and was then added dropwise to 50 mL ice-cold water in 30 min under mechanical stirring. Finally, the suspension was centrifuged, the solid product was collected and washed at least three times with ice water, then dried at 80 °C for 12 h under the vacuum. The sulfonated C-SBA-15 samples with the different sulfonating time were denoted as SC-SBA-15_3h, SC-SBA-15_6h, and SC-SBA-15_9h, respectively.

2.2.2 Preparation of the Ru/SC-SBA-15 Catalysts

The supported Ru catalysts were prepared by the conventional incipient wetness impregnation. Typically, 1.0 g SC-SBA-15-6 h was added to 8.0 mL ethanol with three drops of hydrochloric acid. And then 4.0 mL ethanol solution of $RuCl_3$ (7 mg·mL^{-1}) was added the above solution under vigorous stirring. After continuous stirring vigorously at 50 °C about for 12 h, the solvent was removed by evaporation at 80 °C, yielding a solid powder. The as-prepared powder was transferred into a crucible and then placed into a quartz tube furnace maintaining 300 °C for 2 h under flowing H_2 atmosphere with a heating rate of 2.5 °C·min^{-1} prior to the characterization and reaction. The resulting catalyst was denoted as Ru/SC-SBA-15_6h. Additionally, Ru/SC-SBA-15_3h and Ru/SC-SBA-15_9h were synthesized in a similar method. Ru/C-SBA-15 catalyst (no sulfonation) was also prepared using C-SBA-15 as a support for the sake of comparison.

To get a deep insight into the role of -SO_3H group in the Ru/SC-SBA-15_6h catalyst, in another control experiment, the proton of -SO_3H group was removed selectively by the ion exchange with NaCl aqueous solution [36]. Afterwards, the resulting catalyst (Ru/SC-SBA-15_6h_E) was employed for FFR hydrogenation.

2.2.3 Catalyst Characterization

Powder X-ray diffraction (XRD) analysis of the samples were collected on a Rigaku D/MAX 2550 VB/PC instrument equipped with a 9 kW rotating anode Cu source at 45 kV and 100 mA (0–5°, 5–75°, 0.2° s^{-1}). Raman spectroscopy was performed using a Thermo Scientific DXR Raman microscope equipped with a 532 nm laser excitation source operated at 25 mW. Quanta chrome NOVA 2200e equipment was used to perform BET surface area analysis at − 196 °C with liquid nitrogen. Nitrogen physisorption was performed after degassing at 200 °C for 5 h to a vacuum of 10^{-3} Torr before analysis. The pore size distribution from the adsorption isotherm was calculated by the BJH method. Thermo Scientific ESCALAB 250 was used to perform X-ray photoelectron spectroscopy (XPS) analysis. Field emission scanning electron microscopy (FESEM) images were performed on JSM electron microscopes (JEOL JSM-6360LV, Japan). High angle annular dark field scanning TEM (HAADF-STEM) was performed on a Talos F200X G2/Talos F200X G2 transmission electron microscope operating at 200 kV with a nominal resolution of 0.16 nm. At least 150 Ru particles were counted for particle size distribution analysis. The samples for HAADF were prepared by dropping the ethanol solutions containing the NPs onto the holey carbon-coated Cu grids. Water contact angle (CA) was carried out by the Contact Angle Meter (CA100C, Innuo Company, Shanghai, China) using the droplet profile as a method. The CA was determined using a tangent placed at the intersection of the liquid and solid. A water droplet with a volume of 2 μL was dispensed by a piezo doser onto each sample disk. A CHNS elemental analyzer (Vario MICRO cube) was used to perform elemental analysis. The inductively coupled plasma atomic emission spectroscopy (ICP-AES) analysis was carried out on a Varian ICP-710ES instrument. The acidities of the -SO_3H group were measured by the ion exchange method [36]. Briefly, 0.1 g catalyst was mixed with 5 mL of 1 mol·L^{-1} NaCl solution and stirred at room temperature for 4 h. The protons of the -SO_3H group were selectively exchanged with Na^+ and was then released into the solution. The suspension was filtered and the concentration of H^+ in filtrate was then measured by titration with 0.01 mol·L^{-1} of NaOH solution using phenolphthalein as an indicator. Total acidity was also measured through a similar process. Specifically, 0.1 g of catalyst was mixed with 5 mL of 0.01 mol·L^{-1} NaOH solution. After sufficient mixing and filtration, total acid density was titrated by 0.01 mol·L^{-1} HCl using phenolphthalein as an indicator.

2.3 Catalytic Reactions

The hydrogenation reaction was performed in batch stainless steel autoclave with a 20 mL polytetrafluoroethylene liner. The autoclave was equipped with gas supply system and a magnetic stirrer. In a typical procedure, a certain amount of catalyst was dispersed in 5.0 mL water, and then put into a certain amount of FFR. After purging with hydrogen for three times. The autoclave was sealed with the required hydrogen pressure and heated to the specified temperature in 25 min. Reaction time started after the set temperature was attained. After the reaction was finished, the reactor was quenched in an ice-water bath to stop the reaction. Straight after, the catalyst was separated from the solution by filtration. The products in aqueous phase were extracted by diethyl ether several times and analyzed by GC and MS on Shimadzu GC-2014 equipped with an KB-50 MS (30 m long, 0.32 mm i.d., 0.50 μm film thickness) and an Agilent 6890/5973 GC–MS system equipped with a HP-5 MS column (30 m long, 0.25 mm i.d., 0.25 μm film thickness) using *n*-butanol as the internal standard. All the products were identified by GC–MS. The quantitative determination of FFR, FAL, THFA, 1,4-PeDO and 5-hydroxy-2-pentanone (5-HP) was performed with the authentic samples by GC using individual calibration curve method (Figs. S1–S5) and thus the correction factors were obtained accordingly. The conversion of substrates and yield towards products were calculated as follows:

$$\text{Conversion}\ (\%) = \frac{\text{Amount of substrates converted (mole)}}{\text{Amount of substrate taken (mole)}} \times 100\% \quad (1)$$

$$\text{Yield}\ (\%) = \frac{\text{Amount of a product formed (mole)}}{\text{Amount of substrate taken (mole)}} \times 100\% \quad (2)$$

The catalytic experiments were repeated three times, and the standard deviations for the conversion and yield were within ± 3%. The recyclability of the Ru/SC-SBA-15_6h catalyst was evaluated in six consecutive runs at 140 °C and 1.5 MPa. Briefly, the hydrogenation of FFR was operated in a high-pressure batch autoclave of stainless steel with a 20 mL polytetrafluoroethylene liner. After reaction, the catalyst was washed with ethanol and water several times to remove the products, followed by drying at 80 °C for 10 h. Then the dried catalyst can be used for the next run.

In kinetic studies, MATLAB program has been used for solving the ordinary differential equations as indicated in the section of results and discussion, and the kinetic parameters k_1-k_8 were determined accordingly. The function of lsqnonlin nonlinear fitting in MATLAB was also adopted to minimize the error between experimental and predicated data. The obtained reaction rate constants were then employed to evaluate the apparent activation energy (E_a) by plotting lnk versus 1000/T through Arrhenius equation.

3 Results and Discussion

3.1 Catalyst Characterization

The conversion of FFR to diols involves hydrogenation, ring-opening and de-oxygenation, in which the acid sites and metal sites have a significant effect on the activity and selectivity of FFR hydrogenation [13, 27, 37, 38]. However, the effect of acid density on the selectivity of products has not been investigated thoroughly in FFR hydrogenation. In this work, the carbon layer coated on SBA-15 was firstly sulfonated with concentrated sulfuric acid, and then Ru species was introduced with low loading (*ca.* 1 wt%). As shown in Table S1, the C and H contents of the as-prepared catalysts have been determined by elemental analysis and the S, Ru and Si contents by ICP-AES, respectively. This further confirms that sulfonic acid groups were incorporated on the catalysts surface after the H_2SO_4 treatment and the sulfonating did not exert any impact on a sequential loading of Ru species.

The small-angle and wide-angle XRD patterns (Inset) of the Ru-based catalysts are shown in Fig. 1. It was observed that from small-angle XRD patterns, all the samples except Ru/SC-SBA-15_9h presented an intense (100) reflection and two less intense (110) and (200) reflections, appearing at 2θ = 0.5–1.1° and 2θ = 1.3–2.1° respectively, which were characteristic of the hexagonal p6mm symmetry of SBA-15 [39], while Ru/SC-SBA-15_9h showed only (100) peak.

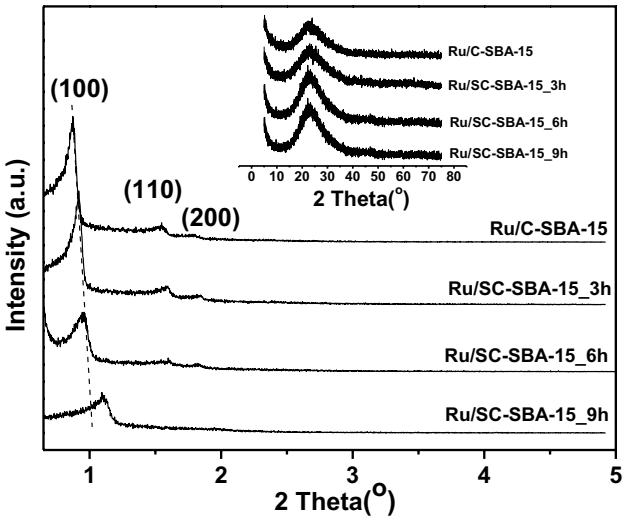

Fig. 1 XRD patterns of the different Ru-based catalysts

These results indicated that the porous structure of SBA-15 was preserved regardless of carbon doping, sulfonation and the sequential fabrication of Ru species. However, with the extension of sulfonation time, the (100), (110) and (200) diffraction peaks of Ru/SC-SBA-15 catalysts shifted to higher angle. Especially, Ru/SC-SBA-15_9h shifted to a much larger extent likely due to the formation of more sulfonic groups by sulfonating and thus the mesoporous structure of SBA-15 was influenced to some extent. Next, the wide angle XRD patterns were also presented in Fig. 1 (insert), it could be seen that Ru-based catalysts showed a broad diffraction peak at 2θ = 23.0° that was assigned to the amorphous silica. Moreover, with the increase of sulfonating time, there was no obvious changes among these diffraction peaks of the samples, while the peak at 24° and 43° assigned to carbon structures were almost indiscernible due to the low content of carbon materials on the SBA-15 [34]. Particularly, the diffraction peaks from Ru species were almost not observed in all samples, indicating that Ru species are highly dispersed on the support surface or beyond the XRD detection limit [40].

Raman spectroscopy was very sensitive to subtle structural variations in carbon materials. Thus Ru/SC-SBA-15_6h and Ru/C-SBA-15 catalysts were characterized by Raman spectroscopy. As shown in Fig. S6, it could be observed clearly that sulfonation has no effect on the structure of the carbon layer and two strong peaks at 1358 cm^{-1} and 1598 cm^{-1} can be assigned to the D and G bands of the disordered and graphitized carbons, respectively [41, 42]. In addition, the second-order (2D) band was the most prominent feature in the Raman spectrum of graphene, and its shapes is sensitive to the number of layers of graphene. From Fig. S6, a very sharp 2D band was observed at

approximately 2753 cm^{-1} for Ru/SC-SBA-15_6h and Ru/C-SBA-15, and the sharp of 2D band (more specifically the absence of a typical graphite shoulder) was characteristic feature of few-layered graphene [43, 44].

Then, the structure of catalysts was further studied by the nitrogen adsorption–desorption method. Fig. S7 showed the nitrogen adsorption–desorption isotherms and pore size distribution of the Ru-based catalysts. As shown from Fig. S7, all the Ru-based catalysts exhibited IV-type isotherms with H1 hysteresis loops at the relative pressure between about 0.6 and 0.8 while the support was laced with carbon and sulfur, indicating that the mesopores were relatively uniform in size and with a center of about 7.5 nm (Fig. S7, insert). The corresponding texture properties (BET surface area, pore diameter and total pore volume) are also shown in Table 1. The BJH pore size distribution also showed that the samples did exhibit the ordered pores. Especially, the Ru/C-SBA-15 showed the highest surface area, total pore volume and pore size among the Ru-based catalysts. With the increase of the sulfonation time, the resulting samples afforded obvious decreases of the surface areas, total pore volume and pore size because the pores of the catalysts were partly blocked by the sulfonic groups. For example, the BET surface area, pore volume and pore diameter of Ru/SC-SBA-15_9h were decreased considerably, as compared with other Ru catalysts (Table 1), revealing that the doping of more sulfonic groups caused a dramatic shrinkage of the mesoporous structure. Besides, as shown in Table 1, the sole carbonization process was also accompanied with emerge of oxygen-containing groups, such as –OH and –COOH, on the C-SBA-15 sample (total acid 0.24 $mmol \cdot g^{-1}$). However, after sulfonation, the amount of sulfonic groups increased considerably on the basis of ICP-AES or a titration analysis, which afforded a similar results (Table 1). It should be noting that the present sulfonation process not only introduced -SO_3H groups, but also led to an increase of total acidity (Table 1), where the other acidic functional groups besides -SO_3H group, including carboxylic and hydroxyl groups [36].

The XPS characterizations were employed to investigate the surface valence state of the catalysts. As shown in Fig. 2, the high resolution XPS spectra of Ru 3p revealed the surface characteristics of the Ru species, and the spectra were calibrated using carbon at 284.4 eV. For Ru/C-SBA-15, the intense doublet peaks of 3p3/2 and 3p1/2 for Ru^0 appeared at 461.8 and 483.8 eV, while the weak 3p3/2 and 3p1/2 peaks appeared at 464.2 and 486.6 eV were attributed to Ru^{n+} [45, 46]. Comparatively, the surface Ru NPs were in an electron-poor state as compared with the sulfonic group. If the interaction existed between the sulfonic group and Ru species, the electron transfer occurred between two species. Then, the binding energy of the surface ruthenium atoms would move to a lower value [45]. In fact, as compared with the Ru 3p3/2 and 3p1/2 binding energy of the Ru/C-SBA-15 (Fig. 2), either Ru^0 or Ru^{n+}, that of Ru/SC-SBA-15_6h (Ru^0: 461.1 and 483.3; Ru^{n+}: 463.8, 486.1 eV) were indeed shifted

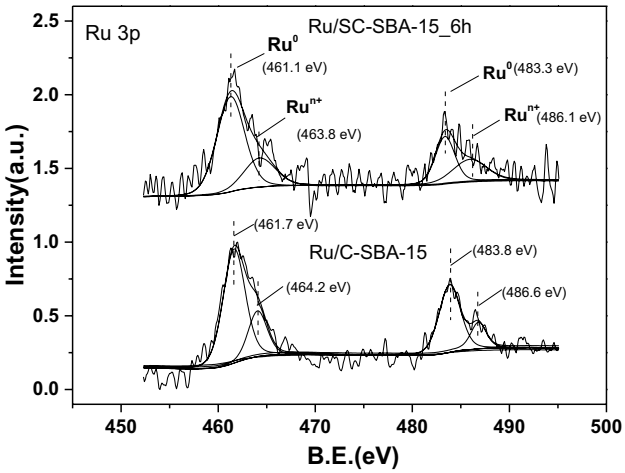

Fig. 2 XPS spectra of Ru 3p of Ru/C-SBA-15 and Ru/SC-SBA-15_6h

Table 1 Physical properties of different Ru catalysts

Catalysts	S_{BET}[a] ($m^2 \cdot g^{-1}$)	V_{total}[b] ($cm^3 \cdot g^{-1}$)	Pore size[c] (nm)	Total acid density[d] ($mmol \cdot g^{-1}$)	-SO_3H Density[e] ($mmol \cdot g^{-1}$)	Acid density[f] ($mmol \cdot g^{-1}$)
Ru/C-SBA-15	602	0.91	7.8	0.24	–	–
Ru/SC-SBA-15_3h	526	0.84	7.6	0.49	0.12	0.09
Ru/SC-SBA-15_6h	453	0.76	7.3	0.81	0.29/(0.22)	0.23
Ru/SC-SBA-15_9h	368	0.70	7.1	1.12	0.48	0.39

[a]Surface area was calculated from the nitrogen adsorption isotherm using the BET method

[b]Total pore volume was calculated from nitrogen sorption isotherms at $P/P_0 = 0.99$

[c]Pore size was calculated by the BJH method

[d]Total acid and

[e]The proton acid of the -SO_3H group were determined by a titration method, respectively [36]. The values in the parenthesis referred to the acid amount ($mmol \cdot g^{-1}$) of the catalyst after recycling for six times

[f]The amount of -SO_3H groups was calculated on the basis of ICP-AES analysis (Table S1)

toward lower binding energy significantly (about 0.5 eV), implying that the specific interaction could endow Ru sites with higher electron density.

Simultaneously, C 1s and Ru 3d of Ru/C-SBA-15 and Ru/SC-SBA-15_6h were shown in Fig. 3, and the spectra were calibrated using silicon at 103.4 eV. It could be observed that C 1s spectra of Ru/C-SBA-15 exhibited three deconvoluted binding energy peaks: the strong peak at 284.5 eV was ascribed to the aromatic carbon (sp^2 carbon), the peak at 286.5 eV corresponded to carbonyl (C=O) and the peak at 288.3 eV was ascribed to carboxylic group (−COOH), respectively (Fig. 3a) [47, 48]. C 1s of Ru/SC-SBA-15_6h exhibited no obvious changes, as compared with that of Ru/C-SBA-15, which confirmed that the oxidation state of the elements remained unchanged after the H_2SO_4 treatment. Notably, Ru 3d5/2 peak of Ru/C-SBA-15 appeared at 281.7 eV belonged to Ru^0 [49]. The binding energies of Ru 3d5/2 of Ru/SC-SBA-15_6h was also shifted to lower value (281.1 eV) due to the introduction of sulfonic groups, which also suggested that the sulfonic acid on the carbon layer could coordinate with Ru species and thus might donate electron density to active Ru sites on the support, in line with that of the Ru 3p spectra above (Fig. 2).

Based on the characterizations by elemental analysis, XRD, Raman and XPS, it indicated that a large amount of sulfonic groups was generated on the carbon layers and the dispersed Ru species could be preferentially coordinated with sulfonic groups. Next, the morphology of carbon coated on SBA-15 and the sulfonated carbon layers coated SBA-15 supports needed to be identified by SEM. As shown in Fig. 4a, SEM images of Ru/C-SBA-15 displayed a uniformly fibrous macroscopic structure with relatively uniform size of 200–400 nm. Comparatively, the sulfonated Ru-based catalysts showed a slight collapse of mesoporous structure, as compared with that of Ru/C-SBA-15 although they also exhibited the similar rope-like units in the 200–500 nm diameter range (Fig. 4b–d). However, the mesoporous structure could be damaged more obviously as the sulfonating

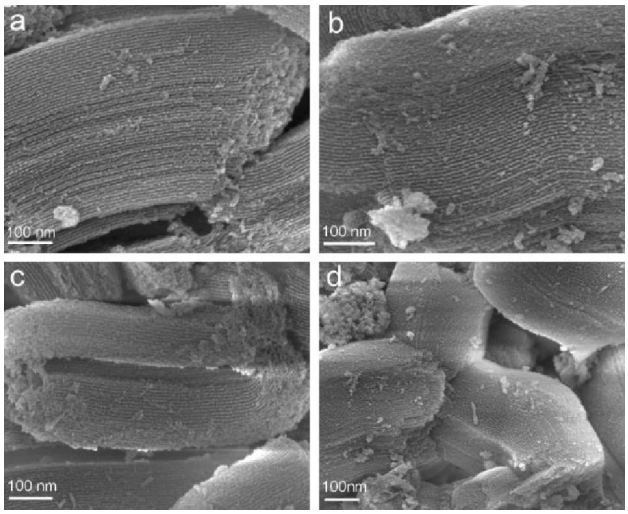

Fig. 4 FESEM images of different Ru-based catalysts. **a** Ru/C-SBA-15, **b** Ru/SC-SBA-15_3h, **c** Ru/SC-SBA-15_6h and **d** Ru/SC-SBA-15_9h

time was extended to 9 h (Fig. 4d). Actually, as evidenced by N_2 adsorption–desorption measurement, the Ru/SC-SBA-15_9h catalyst displayed a partial collapse of pore structure (Table 1).

Subsequently, the dispersion of Ru particles on a sulfonated carbon layer coated SBA-15 was identified by high-angle annular dark-field scanning transmission electron microscopy (HAADF-STEM) images and provided further evidence (Fig. 5). Ru particles on a carbon modified support (Ru/C-SBA-15) had a slight aggregates and uneven distribution owing to weak interaction between carbon and Ru species (Fig. 5a), and the mean size of Ru particles was about 3.2 nm. Nevertheless, once introducing SO_3H groups (Ru/SC-SBA-15_3h), the degree of aggregation with Ru was greatly mitigated and the size of Ru NPs decreased to 1.8 nm (Fig. 5b). It was surprising to find that the average particle size on Ru/SC-SBA-15_6h catalyst was only

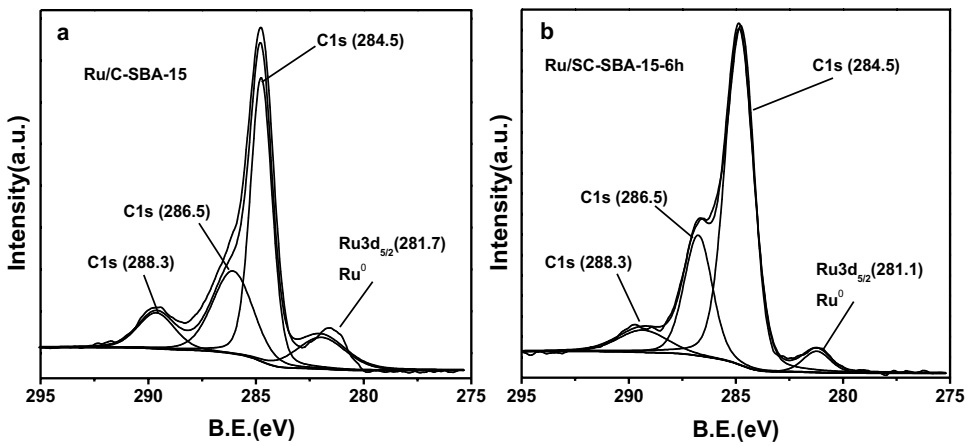

Fig. 3 XPS spectra of **a** C 1s of Ru/C-SBA-15 and **b** Ru/SC-SBA-15_6h

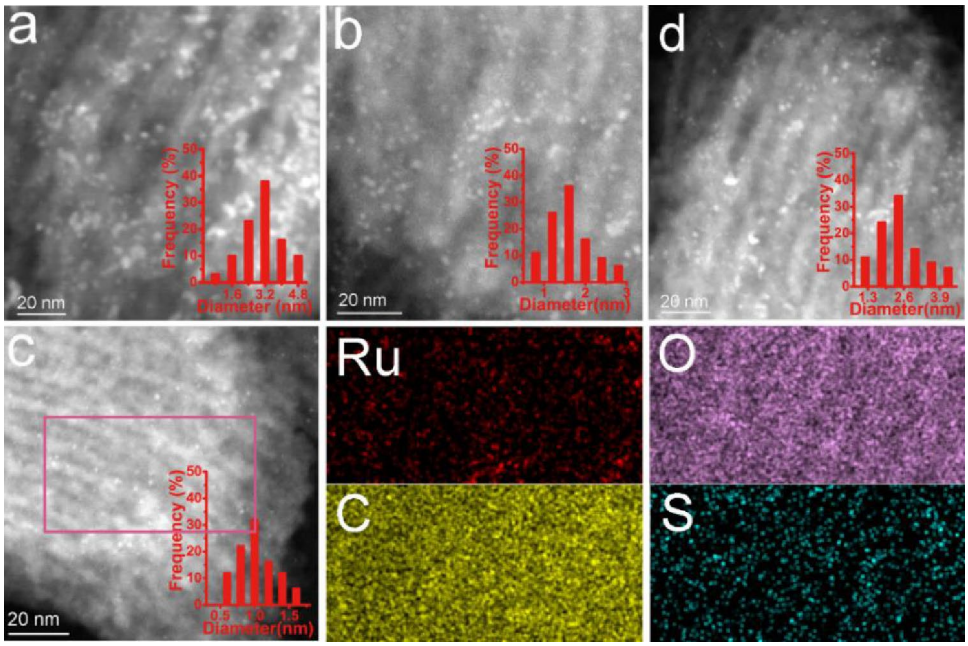

Fig. 5 HAADF-STEM images and the particle size distribution of **a** Ru/C-SBA-15, **b** Ru/SC-SBA-15_3h, **c** Ru/SC-SBA-15_6h and corresponding EDS elemental mappings of Ru, O, C, S; **d** Ru/SC-SBA-15_9h

1.0 nm. Simultaneously, the fine Ru particles were dispersed uniformly on the surface of the catalyst and had almost no aggregation even after the reduction process (Fig. 5c), likely resulting from the synergistic role of -SO_3H groups and mesoporous structure of SBA-15. Besides, the corresponding elemental mapping also confirmed that Ru species were indeed distributed homogeneously on the sulfonated support and actually were consistent with that of C and S elements. Combination of XPS and STEM characterization (Figs. 2 and 5), there was the electronic interaction of the Ru species with the adjacent -SO_3H groups, which could prevent the nanosized Ru particles from the aggregation in the course of catalyst preparation. As such, the possible coordination between Ru centers and the adjacent sulfonic acid groups on the catalyst surface occurs and has been depicted in Fig. S8. On the other hand, SC-SBA-15_6h catalyst with the high BET area would also favor for dispersion of metal species [34]. Unfortunately, when the sulfonation time exceeded 9 h, Ru NPs partially aggregated and Ru particles grew to 2.5 nm (Fig. 5d). This was because an excessive sulfonation will destroy pores of SBA-15 partially, which caused a loss of porous structure (Table 1).

In the next step, the surface hydrophilicity of the different Ru-based catalysts were evaluated by using static water contact angle (WCA). One hand, it can be seen that Ru/C-SBA-15 catalyst was rather hydrophilic (WCA was only 29°) even without sulfonation due to the presence of surface polar groups like (–OH, –COOH). On the other hand, as shown in Fig. S9, WCAs became even smaller as the sulfonating time increased. These results clearly demonstrated that the hydrophilicity of the carbon materials was further enhanced by treating with concentrated sulfuric acid due to the formation of more hydrophilic functional groups (–OH, –COOH, –SO_3H) on the surface of the catalysts in line with the previous titration analysis.

3.2 Hydrogenation of FFR

3.2.1 The Role of Surface Sulfuric Acid Groups on the Ru Catalysts

Firstly, the different Ru catalysts have been used for the hydrogenation of FFR under the identical reaction conditions in aqueous phase. As shown in Table 2, Ru/C-SBA-15 catalyst provided a full conversion of FFR, indicating that the Ru sites on the catalyst were easily accessible to FFR. However, the FAL and THFA were produced in a large amount arising from the reduction of aldehyde group and furan ring of FFR molecules along with the formation of a wide range of the other products, but 1,4-PeDO was formed with only 36% yield (Table 2, entry 1). This revealed that the weak acid sites (–OH or –COOH groups) were insufficient to open the furan ring efficiently, and sequentially did not initiate the production of 5-hydroxy-2-pentanone (5-HP) and 1,4-PeDO. In addition, a small amount of 2-methylfuran (2-MeTHF) was detected by GC–MS, likely arising from hydrodeoxygenation of THFA. These results demonstrated that although Ru/C-SBA-15 exhibited high hydrogenation activity by virtue of the mesoporous structure and active Ru sites, the yield of 1,4-PeDO was rather poor owning to the absence of appropriate acid sites.

However, if the sulfonated Ru/SC-SBA-15_6h catalyst with appropriate sulfonic acid density (0.29 mmol·g^{-1}, Table 1) was employed for hydrogenation of FFR.

Table 2 Hydrogenation of furfural over different catalysts

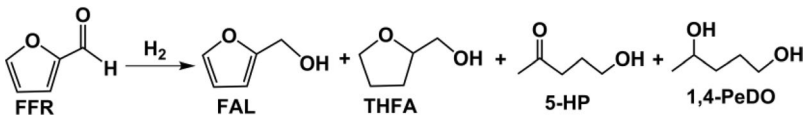

Entries	Catalysts	Yield (%)				
		FAL	THFA	5-HP	1,4-PeDO	Others
1	Ru/C-SBA-15	8	26	18	36	12
2	Ru/SC-SBA-15_6h	–	7	–	87	6
3[a]	Ru/C-SBA-15 + *p*-TsOH	–	19	8	63	10
4[a]	Ru/C-SBA-15 + H_2SO_4	–	15	11	55	19
5[a]	Ru/C-SBA-15 + CF_3SO_3H	–	16	10	59	15
6[b]	Ru/SC-SBA-15_6h_E	4	22	14	51	9
7[c]	Ru/SC-SBA-15_6h + NaOH	20	34	–	–	46
8	5%Ru/AC[d]	–	67	–	–	33

Reaction conditions: 2 mmol furfural, 20.0 mg catalyst, 140 °C, 1.5 MPa H_2, 4 h and 4.0 mL H_2O. All furfural was consumed nearly completely in the reactions. The reactions were repeated at least 3 times, and the standard deviation of yields is within ± 3%

[a]The molar amount of liquid acid was equivalent to that of Ru/SC-SBA-15_6h (1.78×10^{-2} mmol)

[b]The proton of the -SO_3H group in the catalyst was removed by ion exchange with NaCl

[c]NaOH was added in the equivalent of acid sites in Ru/SC-SBA-15

[d]The commercial 5%Ru/AC catalyst was used 4.0 mg. Others include oligomeric and tar-like products and could not be identified by GC

Comparatively, Ru/SC-SBA-15_6h afforded much higher yield of 1,4-PeDO than that of Ru/C-SBA-15 catalyst, indicating the crucial role of the sulfonic acid groups. The yield of 1,4-PeDO increased up to 87%, and meantime the formation of by-products was suppressed significantly (Table 2, entry 2). Especially, Ru/SC-SBA-15 still afforded a lower activity than that of Ru/SC-SBA-15_6h even if the strong liquid acids were added in the equivalent of acid sites (Table 2, entries 3–5), which suggested clearly that the surface sulfuric acid groups on the catalyst would be more favorable for producing 1,4-PeDO, as compared with that of the Brönsted acid in the aqueous phase. Notably, when the proton of –SO_3H group in Ru/SC-SBA-15_6h catalyst were exchanged selectively into Na^+ and was then released into the solution, the resulting Ru/SC-SBA-15_6h_E catalyst only showed a 1,4-PeDO yield of 51% (Table 2, entry 6). It should be noting that Ru/SC-SBA-15_6h_E catalyst still gave a slight higher yield of 1,4-PeDO than that of Ru/C-SBA-15, which could be caused by the role of weak acid sites (-COOH, -OH etc.) in promoting the reaction, as indicating in the previous report [13, 27]. Moreover, if the total acid sites were neutralized with the equivalent NaOH, no 1,4-PeDO was found and only FAL (in 20% yield) and THFA (in 34% yield) were detected by GC, along with the unidentified products likely arisen from the polymerization of FFR and the other intermediate species (Table 2, entry 7) [50, 51]. Similarly, the commercial Ru/AC catalyst only gave THFA without opening ring under the same condition. These results proved clearly that the strong acid sites (-SO_3H) were crucial for selective hydrogenation of FFR into 1,4-PeDO, but the role weak acidic sites (-OH and -COOH) cannot be excluded.

Based on all the results above, it was demonstrated that that there might be a coordination interaction between surface acidic groups and the adjacent Ru sites, where the electron transfer from the sulfonic groups to Ru sites occurred, as evidenced by XPS, STEM image and its elemental mappings (Figs. 2, 3 and 5). It should be noting that the electron-rich Ru sites could facilitate adsorption and homolytic dissociation of H_2 [26]. The adjacent Brönsted acid sites were responsible for opening the furan ring, and thus the active hydrogen atoms led to the facile hydrogenation of the intermediates. Overall, the synergistic effect between a surface Brönsted acid sites and Ru sites promoted the FFR hydrogenation and resulted in a high 1,4-PeDO yield.

Next, the effect of surface sulfonic acid group on the FFR hydrogenation has been investigated. As shown in Fig. 6, it was worth noting that all Ru-based catalysts can afford full conversion of FFR under the present condition, and it was observed that sulfonic acid group on the catalyst had a great impact on the distribution of products. Ru/C-SBA-15 with the low acid amount gave only around 36% yield to 1,4-PeDO in FFR hydrogenation. As sulfonic acid density increased to 0.29 mmol·g^{-1}, the yield of 1,4-PeDO achieved the optimum (87%), and the further increasing sulfonic acid density to 0.48 mmol·g^{-1} would result in a sharp decrease

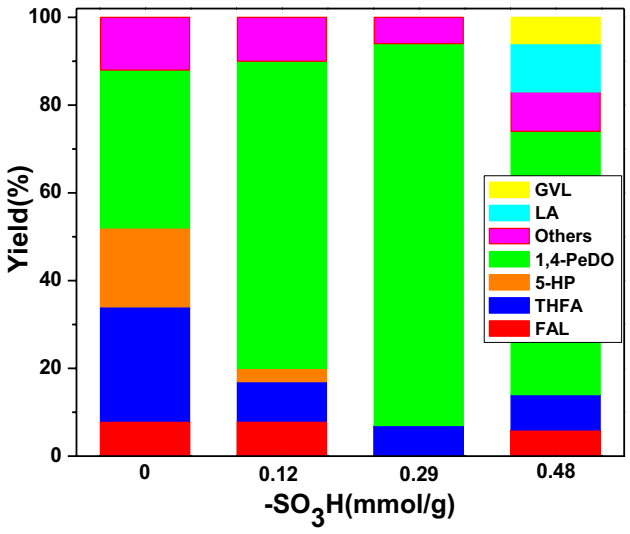

Fig. 6 Effect of the -SO_3H densities on product distribution for the FFR hydrogenation**.** Conditions: 2.0 mmol furfural, 20.0 mg catalysts, 1.5 MPa H_2, 140 °C, 4 h and 4.0 mL H_2O. FFR: Furfural; FAL: furfuryl alcohol; THFA: tetrahydrofurfuryl; 1,4-PeDO: 1,4-pentanediol; 5-HP: 5-hydroxy-2-pentanone; LA: levulinic acid, GVL: γ-valerolactone

in yield of 1,4-PeDO. This can be explained by following reasons. Firstly, excessive acid sites would promote more by-reactions like polymerization, acid hydrolysis, leading to LA, GVL and other side-products in a considerable amounts, which decreased the selectivity to 1,4-PeDO significantly. Secondly, the excessive sulfonation would lead to the partial collapse of mesoporous structure of SBA-15 (Fig. 4d), along with a decrease of BET surface area (Table 1, entry. 4), which might restrict the hydrogenation of the intermediate products to some degree. Third, the excessive sulfonation might result in too strong hydrophilicity of catalyst (Fig. S9d), it might be not favorable due to competitive adsorption of the substrate and water molecules. Therefore, Ru/SC-SBA-15_6h with the sulfonic acid density of 0.29 $mmol{\cdot}g^{-1}$ gave the optimum result for the selective hydrogenation of FFR into 1,4-PeDO under the present condition.

Figure S10 showed conversion/time profiles and yield of 1,4-PeDO/time profiles of hydrogenation reactions catalyzed by the different Ru catalysts at 140 °C. It was found that Ru/SC-SBA-15_6h catalyst indeed afforded the highest FFR conversion and the yield of 1,4-PeDO among the catalysts used in this work. This suggested that Ru/SC-SBA-15_6h catalyst owned the appropriate acid sites and fine-dispersed metal sites, and a good match between two sites has been achieved, which were required to promote the formation of 1,4-PeDO. In other words, the ordered mesoporous structure, and the electronic interaction between the sulfonic groups and metal Ru species were the decisive factors for the selective conversion of FFR into 1,4-PeDO in the present system. As such, the present catalyst provided high 1,4-PeDO yield (87%) and a full conversion of FFR under rather mild conditions, and the catalytic performance was comparable with or better than that of the previous report [13, 27, 29].

3.2.2 Kinetics and Reaction Pathway

To get a deep insight into the reaction pathway observed with the present Ru catalyst, the effect of the reaction temperature on product distribution has been evaluated thoroughly. As depicted in Fig. 7a, FFR was converted completely at 80 °C within 8 h, but FAL and THFA were formed as the dominant products, accompanied by a small amount of 5-HP, 1,4-PeDO and 1,2-PeDO. As reaction time was prolonged to 10 h, the FAL yield decreased gradually with a concomitant increase of the THFA (yield up to 32%), and meantime THFA or a part of FAL could be further converted to 1,2-PeDO and 5-HP. When the reaction was carried out at 100 °C, the reaction rates increased and the product yields showed the similar tendency with that of Fig. 7a at the beginning of 6 h (Fig. 7b). However, the yield of 1,4-PeDO rose gradually with the consumption of 5-HP. As the reaction continued on, the dominant products was 1,4-PeDO, accompanied by a trace of 1, 2- PeDO.

As the reaction temperature was further increased to 120 °C (Fig. 7c), FFR was consumed completely within 4 h, and the main product was 1,4-PeDO. On the other hand, the product from THFA dehydration, namely 2-MeTHF started to appear. The by-product 1,2-PeDO is almost undetectable by GC. Finally, the catalytic performance was examined at 140 °C (Fig. 7d). To our surprise, the conversion of FFR reached 100% only within 1.5 h, the main products were 1,4-PeDO along with the intermediate FAL and 5-HP. As the reaction time was prolonged to 4 h, the yield of 1,4-PeDO reached highest (87%), and a small amount of THFA and 2-MeTHF were also detected. However, if the reaction temperature continued to increase to 150 °C, the yield of 1,4-PeDO remained almost unchanged. Meantime, the yield of THFA decreased slightly, along with forming 2-MeTHF from the dehydration of THFA (Table S2). Hence, these kinetic profiles clearly revealed that the catalytic process involves the following sequence (1) the hydrogenation of FFR to FAL followed by (2) the conversion of FAL to 5-HP or THFA and then (3) the hydrogenation of 5-HP or THFA to 1,4-PD.

Next, Based on the product distribution, a skeleton reaction network related to FFR conversion over Ru/SC-SBA-15_6h was constructed (Scheme 1). k_1 was the rate constant from FFR to FAL; k_2 was the rate constant from FAL to THFA; k_3 was the rate constant from FAL to 1,2-PeDO; k_4 was the rate constant from FAL to 5-HP; k_5 was the rate constant from THFA to 2-MeTHF; k_6 was the rate constant from 1,2-PeDO to 1,4-PeDO; k_7 was the rate constant from 5-HP to 1,4-PeDO;

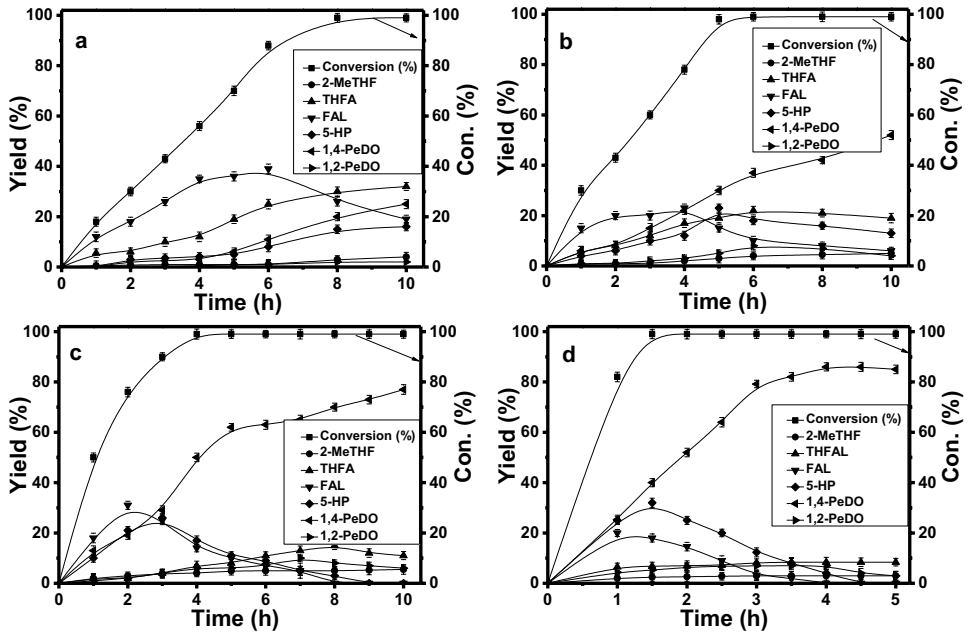

Fig. 7 FFR conversion of and product yield/time profiles of hydrogenation reactions catalyzed by Ru/SC-SBA-15_6h catalyst at different temperatures (bars denote standard deviations). Conditions: 2.0 mmol furfural, 20.0 mg Ru/SC-SBA-15_6h, 1.5 MPa H_2 and 4.0 mL H_2O, **a** 80 °C, **b** 100 °C, **c** 120 °C and **d** 140 °C. FFR: Furfural; FAL: furfuryl alcohol; THFA: tetrahydrofurfuryl; 1,4-PeDO: 1,4-pentanediol; 5-HP: 5-hydroxy-2-pentanone; 1,2-PeDO: 1,2-pentanediol; 2-MeTHF: 2-methylfuran

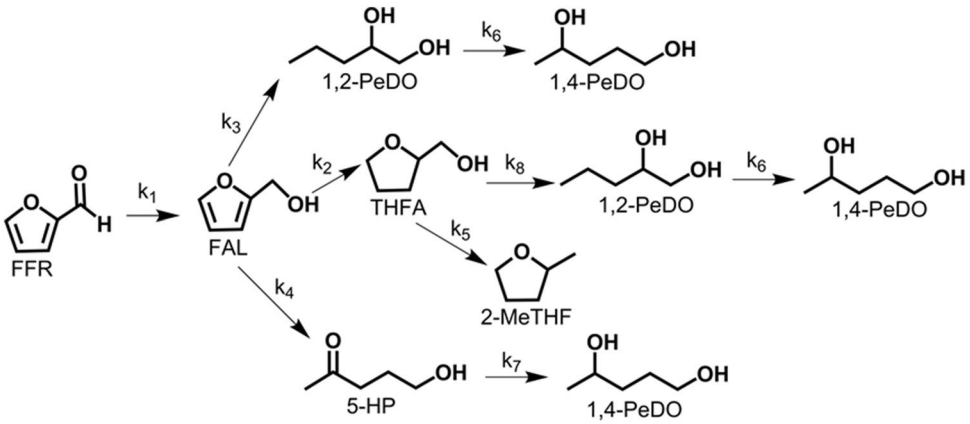

Scheme 1 Reaction pathways of furfural hydrogenation on the Ru/SC-SBA-15_6h catalyst

and k_8 was the rate constant from THFA to 1,2-PeDO. All reactions were considered as pseudo-first order reactions. In order to obtain the kinetic parameters, we conducted FFR conversion experiments at different reaction temperatures (80, 100, 120, and 140 °C), and recorded the conversion of FFR and the yield of all intermediates and by-products (Fig. 7) for the following kinetics studies.

According to the total reaction path (Scheme 1), the change of products concentrations as a function of time were presented by the following differential equations in the presence of excess of H_2:

$$\frac{dC_{FFR}}{dt} = -k_1 C_{FFR} \tag{3}$$

$$\frac{dC_{FAL}}{dt} = k_1 C_{FFR} - \left(k_2 + k_3 + k_4\right) C_{FAL} \tag{4}$$

$$\frac{dC_{THFA}}{dt} = k_2 C_{FAL} - (k_5 + k_8) C_{THFA} \tag{5}$$

$$\frac{dC_{2\text{-}MeTHF}}{dt} = k_5 C_{THFA} \tag{6}$$

$$\frac{dC_{5\text{-}HP}}{dt} = k_4 C_{FAL} - k_7 C_{5\text{-}HP} \tag{7}$$

$$\frac{dC_{1,2\text{-}PeDO}}{dt} = k_3 C_{FAL} + k_8 C_{THFA} - k_6 C_{1,2\text{-}PeDO} \tag{8}$$

Table 3 Estimated kinetic parameters for furfural conversion

T (°C)	Rate constants ($\times 10^{-3}$ min^{-1})							
	k_1	k_2	k_3	k_4	k_5	k_6	k_7	k_8
80	15.03	1.07	0.09	10.98	0.07	0.02	14.30	0.19
100	20.96	2.51	0.80	19.84	0.61	0.11	22.80	0.79
120	31.03	4.29	2.13	30.22	2.39	1.10	36.80	2.03
140	45.80	11.30	5.05	40.46	6.63	3.81	49.01	4.92
Ea_n (KJ/mol)	21.45	46.30	81.33	26.35	96.12	109.65	25.32	65.03

Reaction conditions: 2 mmol furfural, 20.0 mg Ru SC-SBA-15-6 h, 1.5 MPa H_2 and 4.0 mL H_2O. The standard deviation is within ± 3%

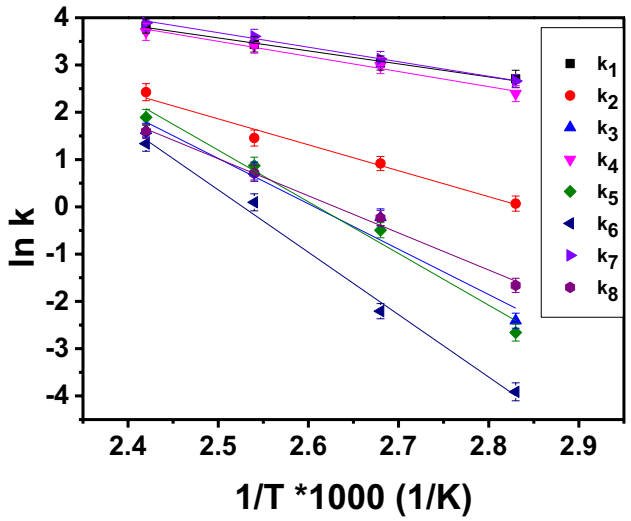

Fig. 8 Arrhenius plots for the hydrogenation reaction of furfural (bars denote standard deviations). The observed rate constants (k) were obtained by fitting with MATLAB at different temperatures according to Fig. 7

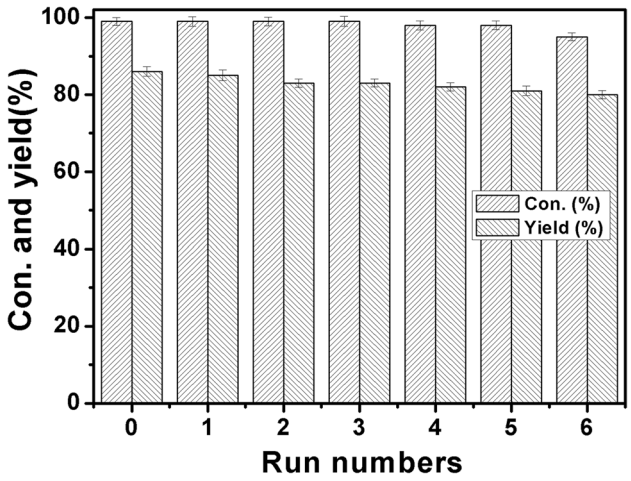

Fig. 9 The recyclability of Ru/SC-SBA-15-6 h for hydrogenation of furfural to 1,4-PeDO (bars denote standard deviations). Reaction conditions: Substrate/Ru = 1000 (molar ratio), 80.0 mg catalysts, 4.0 mL H_2O, 4 h, 1.5 MPa H_2, 140 °C

$$\frac{dC_{1,4\text{ - PeDO}}}{dt} = k_6 C_{1,2\text{ - PeDO}} + k_7 C_{5\text{ - HP}} \quad (9)$$

where the concentrations of FFR, FAL, THFA, 2-MeTHF, 1,2-PeDO, 5-HP and 1,4-PeDO were in mol/L. By solving these ordinary differential equations (ODEs) simultaneously using MATLAB program, the kinetic parameters k_1-k_8 were determined, respectively (Table 3). The function of lsqnonlin nonlinear fitting in MATLAB was also utilized to minimize the error between experimental and predicated data [52].

Then the obtained reaction rate constants were used to evaluate the apparent activation energy (Ea_n) by plotting ln k versus 1/T through Arrhenius equation (Fig. 8). Table 3 summarized the rate constants and activation energies of each reaction. We found that all rate constants increased with temperature increasing. And among all the activation energies of the reactions, Ea_1, Ea_4, and Ea_7 were relatively small compared with other activation energies and below 30 kJ/mol, which demonstrated clearly that the preferential route was the conversion of FFR to FAL, FAL to 5-HP and finally 5-HP to 1,4-PeDO, respectively.

3.2.3 Reusability Test

Next, the reusability of the catalyst was determined because catalyst recyclability exhibited an indispensable part in the economic evaluation of chemical compound transformations. Therefore, we conducted a reusability test on the Ru/SC-SBA-15_6h catalyst, and the result was shown in Fig. 9. After the reaction, the metal Ru catalyst could be separated by a simple filtration. The recovered catalyst was dried for 8 h at 80 °C and then used in the next reaction. As shown in Fig. 9, the catalyst can be reused for at least six consecutive catalytic recycles. The yield of 1,4-PeDO showed a slight decrease, but the activity of the catalyst remained almost unchanged, demonstrating that Ru/SC-SBA-15_6h was highly stable in the aqueous reaction.

The spent Ru/SC-SBA-15_6h catalyst has been characterized for the possible structural changes. As shown in

Fig. S11, the recycling test could not influence the ordered mesoporous structure of the Ru catalyst. Meantime, the sulfonic acid density of the reused catalyst was determined quantitatively by the titration method (Table 1), it was found that even after six catalytic recycles, the sulfonic acidity of the catalyst showed a negligible loss and remained at 0.22 mmol·g^{-1}. It suggested that a sulfonated carbon layer coated SBA-15 was highly water-resistant and the dispersed Ru species was robust for the catalytic hydrogenation likely via a coordination with a sulfonic groups.

Finally, the catalytic performance of the present system was compared with the other earlier reports for the hydrogenation of furfural into 1,4-PeDO. As shown in Table S3, the present bi-functional catalyst can afford the comparable or higher yield of 1,4-PeDO to that of the reported systems. Notably, the present catalytic system was able to catalyze the reaction under milder conditions (short reaction time and low H_2 pressure). Besides, the present catalyst is simple and can be easily available by a conventional method. Meantime, it was highly stable in consecutive catalytic recycles. Inspired by the above results, the design of more-efficient bi-functional catalysts for the catalytic direct conversion of FFR to high-value-added chemicals with high stability is currently underway in our laboratory.

4 Conclusions

In summary, the highly efficient metal–acid bi-functional catalyst has been prepared by using the carbon layer coated C/SBA-15 as a catalyst support, which was then sulfonated with 98% concentrated sulfuric acid, followed by incorporation Ru species. This approach has an advantage in that the acid density was tuned flexibly via controlling sulfonating time. The resulting Ru/SC-SBA-15_6h catalyst have exhibited an excellent catalytic activity (with full conversion of FFR) and high yield of 1,4-PeDO (87%) in selective hydrogenation of FFR under the optimum condition. The detailed characterization demonstrated that both the sulfonic acid group and highly dispersed Ru sites are very crucial for achieving high yield of 1,4-PeDO. Notably, there was a coordination interaction between the sulfonic acid groups and the adjacent Ru sites, which endowed Ru sites with high electron density. The electron-rich Ru sites promoted H_2 dissociation and were beneficial for a sequential hydrogenation of the ring-opining intermediates by acid-hydrolysis. Moreover, such a bi-functional catalyst also exhibited excellent durability. The surface acid density and the ordered mesoporous structure on the catalyst remained no obvious change even after at least six catalytic recycles. The present strategy of introducing Ru species on a sulfonated carbon layer coated SBA-15 to modulate the acidity and metallic bifunctionality of the catalysts could be extended to the transformation of other biomass molecules, thus opening up a new route to produce high-value-added chemicals directly from FFR.

Acknowledgements The authors are grateful for support from the National Natural Science Foundation of China (21773061, 21978095), the innovation Program of Shanghai Municipal Education Commission (15ZZ031).

References

1. Sudarsanam P, Peeters E, Makshina EV, Parvulescu VI, Sels BF (2019) Chem Soc Rev 48:2366–2421
2. Zhou CH, Xia X, Lin CX, Tong DS, Beltramini J (2011) Chem Soc Rev 40:5588–5617
3. Li C, Zhao X, Wang A, Huber GW, Zhang T (2015) Chem Rev 115:11559–11624
4. Zhang Z, Song J, Han B (2017) Chem Rev 117:6834–6880
5. Schutyser W, Renders T, Van den Bosch S, Koelewijn SF, Beckham GT, Sels BF (2018) Chem Soc Rev 47:852–908
6. Alonso DM, Bond JQ, Dumesic JA (2010) Green Chem 12:1493–1513
7. Mariscal R, Maireles-Torres P, Ojeda M, Sádaba I, López Granados M (2016) Energy Environ Sci 9:1144–1189
8. Li X, Jia P, Wang T (2016) ACS Catal 6:7621–7640
9. Nakagawa Y, Tamura M, Tomishige K (2013) ACS Catal 3:2655–2668
10. Chatterjee M, Chatterjee A, Ishizaka T, Kawanami H (2018) RSC Adv 8:20190–20201
11. Liu S, Amada Y, Tamura M, Nakagawa Y, Tomishige K (2014) Catal Sci Technol 4:2535–2549
12. Musci JJ, Merlo AB, Casella ML (2017) Catal Today 296:43–50
13. Liu F, Liu Q, Xu J, Li L, Cui YT, Lang R, Li L, Su Y, Miao S, Sun H, Qiao B, Wang A, Jérôme F, Zhang T (2018) Green Chem 20:1770–1776
14. Mizugaki T, Yamakawa T, Nagatsu Y, Maeno Z, Mitsudome T, Jitsukawa K, Kaneda K (2014) ACS Sustain Chem Eng 2:2243–2247
15. Koso S, Furikado I, Shimao A, Miyazawa T, Kunimori K, Tomishige K (2009) Chem Commun, 2035–2037
16. Koso S, Ueda N, Shinmi Y, Okumura K, Kizuka T, Tomishige K (2009) J Catal 267:89–92
17. Chen KY, Koso S, Kubota T, Nakagawa Y, Tomishige K (2010) ChemCatChem 2:547–555
18. Koso S, Nakagawa Y, Tomishige K (2011) J Catal 280:221–229
19. Koso S, Watanabe H, Okumura K, Nakagawa Y, Tomishige K (2012) Appl Catal B 111–112:27–37
20. Xu W, Wang H, Liu X, Ren J, Wang Y, Lu G (2011) Chem Commun 47:3924–3926
21. Liu S, Amada Y, Tamura M, Nakagawa Y, Tomishige K (2014) Green Chem 16:617–626
22. Li M, Li G, Li N, Wang A, Dong W, Wang X, Cong Y (2014) Chem Commun 50:1414–1416
23. Misugaki T, Nagatsu Y, Togo K, Maeno Z, Mitsudome T, Jitsukawa K, Kaneda K (2015) Green Chem 17:5136–5139
24. Ren D, Wan X, Jin F, Song Z, Liu Y, Huo Z (2016) Green Chem 18:5999–6003
25. Lv J, Rong Z, Sun L, Liu C, Lu AH, Wang Y, Qu J (2018) Catal Sci Technol 8:975–979
26. Cui J, Tan J, Zhu Y, Cheng F (2018) Chemsuschem 11:1316–1320
27. Liu Q, Qiao B, Liu F, Zhang L, Su Y, Wang A, Zhang T (2020) Green Chem 22:3532–3538
28. Rodiansono R, Astuti MD, Hara T, Ichikuni N, Shimazu S (2019) Green Chem 21:2307–2315

29. Ye L, Han Y, Bai H, Lu X (2020) ACS Sustain Chem Eng 8:7403–7413
30. Tang K, Xie S, Cofield GR, Yang X, Tian E, Lin H (2018) Energy Technol 6:1826–1831
31. Yang G, Pidko EA, Hensen EJ (2012) J Catal 295:122–132
32. Lv W, Liao Y, Zhu Y, Liu J, Zhu C, Wang C, Xu Y, Zhang Q, Chen G, Ma L (2020) Cellulose 27:799–823
33. Li T, Lin H, Ouyang X, Qiu X, Wan Z, Ruan T (2020) Fuel 278:118324
34. Qian W, Lin L, Qiao Y, Zhao X, Xu Z, Gong H, Li D, Chen M, Huang R, Hou Z (2019) Appl Catal A 585:117–183
35. Chiang HL, Wu TN, Zeng LX (2019) Microporous Mesoporous Mater 279:286–292
36. Xiao Y, Hill JM (2020) Chemosphere 248:125981
37. Golub KW, Sulmonetti TP, Darunte LA, Shealy MS, Jones CW (2019) ACS Appl Nano Mater 2:6040–6056
38. Pisal DS, Yadav GD (2019) ACS Omega 4:1201–1214
39. Cai X, Wang Q, Liu Y, Xie J, Long Z, Zhou Y, Wang J (2016) ACS Sustain Chem Eng 4:4986–4996
40. Zhang Z, Ding L, Gu J, Li Y, Xue N, Peng L, Zhu Y, Ding W (2017) Catal Sci Technol 7:5953–5963
41. Tian H, Lin Z, Xu F, Zheng J, Zhuang X, Zhuang Y, Feng X (2016) Small 12:3155–3163
42. Wu D, Xu Q, Qian J, Li X, Sun Y (2019) Chem Eur J 25:3105–3111
43. Zheng F, Yang Y, Chen Q (2014) Nat Commun 5:5261–5270
44. Andrea CF, Denis MB (2013) Nat Nanotechnol 8:235–246
45. Zhu W, Yang H, Chen J, Chen C, Guo L, Gan H, Zhao X, Hou Z (2014) Green Chem 16:1534–1542
46. Liu F, Lee JY, Zhou WJ (2006) Small 2:121–128
47. Song Y, Yang J, Wang K, Haller S, Wang Y, Wang C, Xia Y (2016) Carbon 96:955–964
48. Wu ZS, Winter A, Chen L, Sun Y, Turchanin A, Feng X, Mullen K (2012) Adv Mater 24:5130–5135
49. Castro AA, Morales F, Romero M, Conde-Gallardo A, Escamilla R (2018) J Mater Sci 53:8067–8073
50. Pirmoradi M, Janulaitis N, Gulotty RJ Jr, Kastner JR (2020) ACS Omega 5:7836–7849
51. Choura M, Belgacem NM, Gandini A (1996) Macromolecules 29:3839–3850
52. Huang YB, Yang T, Lin YT, Zhu YZ, Li LC, Pan H (2018) Green Chem 20:1323–1334